AIMS Materials Science, 10(2): 227–248.
DOI: 10.3934/matersci.2023013
Received: 30 July 2022
Revised: 18 November 2022
Accepted: 07 December 2022
Published: 07 February 2023

http://www.aimspress.com/journal/Materials

Research article

The performance of radar absorption of $Mn_xFe_{3-x}O_4$/rGO nanocomposites prepared from iron sand beach and coconut shell waste

Yana Fajar Prakasa, Sumari Sumari*, Aman Santoso, Muhammad Roy Asrori and Ririn Cahyanti

Department of Chemistry, Faculty of Mathematics and Natural Sciences, Universitas Negeri Malang, Jl. Semarang No. 5, Malang, 65145, Indonesia

*** Correspondence:** Email: sumari.fmipa@um.ac.id; Tel: +62 81333911567.

Abstract: In this work, the Fe_3O_4 nanoparticles from natural iron sand were doped with Mn and combined with reduced-graphene oxide (rGO) to obtain $Mn_xFe_{3-x}O_4$/rGO nanocomposites with mole fraction variations of the Mn of 0.25, 0.5, and 0.75. The crystalline phase of the synthesized $Mn_xFe_{3-x}O_4$/rGO nanocomposites formed an amorphous phase. The presence of rGO was observed through EDX results. The magnetical properties of $Mn_xFe_{3-x}O_4$/rGO nanocomposites were shown by decreasing the Br, H_cJ, H_{max} along with increasing of Mn doping. Interestingly, increasing rGO and Mn composition made the absorption bandwidth of the $Mn_xFe_{3-x}O_4$/rGO nanocomposites wider, so that the radar absorption also increased marking by the greater reflection loss that reached −11.95 dB. The increase in the radar absorption performance of $Mn_xFe_{3-x}O_4$/rGO nanocomposites came from the efficient complementarity between dielectric loss and magnetic loss and interfacial polarization between Fe_3O_4 doped Mn and rGO.

Keywords: $Mn_xFe_{3-x}O_4$/rGO; iron sand; coconut shell waste; radar absorbing material; simple co-precipitation method

1. Introduction

The development of telecommunications technology certainly cannot be separated from the use

of electromagnetic waves, one of which is radar (radio detection and ranging) waves. The use of radar waves is superior in military applications [1], antenna technology [2], and radar wave processing [3]. Along with the rapid development of technology, several problems were found due to the use of radar. These problems such as electromagnetic wave pollutions [4] and human health problems [5] cause electromagnetic wave interference [6]. In the last decade, some of the above problems can be overcome by the use of radar absorbing material/RAM [7,8]. One example of the application is coating the body of military vehicles such as tanks or military aircraft [9]. Radar transmitted from the source is ensured to be absorbed and dissipated by RAM so that it can reduce the results of radar reflection of radar waves from an object [10].

Generally, RAM works on the principle of combining a dielectric material and a magnetic material, so that the incoming radar wave will be absorbed through an impedance match to a polarizing effect [11,12]. The main ingredients of RAM basically have magnetic and electrical properties that aim to produce magnetic and dielectric losses [13]. Magnetic metal powders, ferrites, and nanotubes are some of the magnetic materials that have high adhesion and density [14,15]. Ferrimagnetic materials such as Fe_3O_4 based on natural iron sand were chosen as magnetic materials, because they have high saturation magnetization, good flexibility [16], heat resistance [12], good chemical and thermal stability [17], high permeability, and low cost of synthesis [18,19]. However, Fe_3O_4 is not sufficient in RAM applications because it only produces a reflection loss (RL) of −5 dB [20]. Thus, it is necessary to have a combination of other materials that can increase the dielectric loss value. Efforts to increase the value of dielectric loss in Fe_3O_4 are generally carried out by doping divalent cations such as Mn^{2+}. This is important, because it provides an opportunity to improve the dielectric and magnetic properties [18,21]. Furthermore, Mn^{2+} has soft magnetic properties which affect the low coercivity field, making it suitable for RAM applications [22–24].

Regarding the methods used in recent years, several synthesis methods were found, namely solid state reaction [25], solvothermal [26], ball milling [27], sol-gel [28], dan co-precipitation [29]. From the various synthesis methods, the co-precipitation method has advantages in the form of economic value, easy to perform, fast processing and relatively homogeneous results [30,31]. Furthermore, the co-precipitation method can be applied to various materials, including natural materials. In this research, $Mn_xFe_{3-x}O_4$ was synthesized by co-precipitation method using natural materials based on iron sand. Iron sand was selected and taken from Bajul Mati Beach because it contains a fairly high magnetite material, which is 90.4% [32,33].

To improve the absorption performance of radar waves, a material with better dielectricity is needed. Previous studies reported that $Mn_xFe_{3-x}O_4$ materials still have limitations, such as low permittivity and complex permeability [24,34]. In addition, one of the main causes of limitations in the application of $Mn_xFe_{3-x}O_4$ RAM is the high density value [18,35], low stability, and small dielectric loss making it difficult to apply as RAM [13].

Carbon-based materials are often used as dielectric materials for RAM purposes because they have advantages such as high electrical conductivity and low density [36,37]. Saeed et al. carried out the synthesis of magnetic nano composites/MWCNT and they obtained excellent wave absorption results [38]. In another study, Taufiq et al. synthesize magnetic materials combined with activated carbon to increase the value of RL [11]. According to the research of Zhao et al., reduced-graphene oxide (rGO) materials can also be combined with magnetic materials for the purpose of increasing reflection loss (RL) [39].

Regarding the selection of rGO, the advantages of rGO include materials with good dielectric

properties, low density, high surface area and good electrical conductivity [40,41], so it is necessary to stabilize the density and dielectric properties of the material from RAM to obtain optimal radar wave absorption capability. Furthermore, the residual and functional group defects cause a polarizing effect that contributes to the increase in the RL value [42]. Thus, in this study, the synthesis of rGO based on coconut shell waste material as a precursor with $Mn_xFe_{3-x}O_4$ was carried out. The choice of coconut shell used as a dielectric material because it has a carbon element with a content that reaches 80 wt% [43], so it is able to absorb radar waves well [44]. Meanwhile, rGO has properties in hydroxyl and carboxyl structural defects that support the absorption of radar waves through the principle of surface polarization [36,40]. In addition, rGO has a low density and reduces the aggression of $Mn_xFe_{3-x}O_4$, making it suitable for use as an antiradar dielectric material [45]. The method used for the synthesis of rGO is solid state reaction, because the method is simple. Then, the process of combining $Mn_xFe_{3-x}O_4$ (x = 0.25, 0.50, 0.75) with rGO in the form of $Mn_xFe_{3-x}O_4$/rGO nano composites through the coprecipitation method. These results present a discussion of the structure, elemental content, morphology, and RAM potential of the $Mn_xFe_{3-x}O_4$/rGO nanocomposite.

2. Materials and methods

2.1. Materials

The materials used in this study were iron sand obtained from Bajul Mati Beach, Malang as the main component for Fe and coconut shell waste obtained from Malang. Then, the powder of manganese(II) chloride hydrate ($MnCl_2{\cdot}4H_2O$, 99.99%, Sigma-Aldrich, Germany), chloride acid (HCl, 99.99%, Merck, Germany), ammonium hydroxide (NH_4OH, 99.99%, Merck, Germany), ethanol (EtOH, 100%, Merck, Germany), distilled water and ultrafiltered water (MQ).

2.2. Synthesis of rGO from Coconut Shell Waste

The rGO material was synthesized using the solid-state reaction method. The process began with the cleaned coconut shell which. The coconut shells were washed with distilled water and dried in the sun for 3 d. After drying, the coconut shell was burned to form charcoal. Furthermore, the charcoal was sieved using a 200 mesh sieve to obtain charcoal powder. Then, the sample was carbonated at 400 ^oC for 5 h.

2.3. Synthesis of $Mn_xFe_{3-x}O_4$/rGO (x = 0.25, 0.50, 0.75)

The $Mn_xFe_{3-x}O_4$/rGO nanocomposite was synthesized using the co-precipitation method with the following steps. In general, the $Mn_xFe_{3-x}O_4$ synthesis procedure has been corresponded in previous studies [21]. At first, the iron sand was washed and dried in the sun to dry. It was then separated using permanent magnets to remove impurities. Next, 20 g of iron sand was dissolved in 58 mL of HCl with a stirring speed of 720 rpm for 30 min at room temperature. The solution was filtered and separated from the residue using filter paper to obtain a solution of $FeCl_2$ and $FeCl_3$. Simultaneously, the rGO powder was dispersed into 50 mL of distilled water and sonicated for 2 h at room temperature. Then, each mole fraction, namely: x = 0.25 was 1.36 g, x = 0.50 was 2.72 g,

x = 0.75 was 4.09 g $MnCl_2{\cdot}4H_2O$ and rGO suspension was added to a mixture of 18 mL of $FeCl_2$ and $FeCl_3$ solution. The mixing process was carried out with a stirring speed of 720 rpm which was then titrated with 25 mL of NH_4OH at room temperature. This synthesis process was carried out for 30 min until a black precipitate was produced. The precipitate was washed repeatedly using distilled water until it was odorless with a pH value of 7. Then, each precipitate was filtered using filter paper and dried in an oven at 100 ℃ for 1 h. After drying, 1.5 g of $Mn_xFe_{3-x}O_4$/rGO material was compacted with manual pressure to become pellets with a diameter of 0.5 cm and thickness of 1 cm. It was sintered at 400 ℃ for 1 h. The synthesized material was characterized by instruments. The rGO samples were coded as rGO and the $Mn_xFe_{3-x}O_4$/rGO samples with various mole fraction x = 0.25, 0.50, 0.75 coded respectively RAM1, RAM2, RAM3 for $Mn_{0.25}Fe_{2.75}O_4$, $Mn_{0.5}Fe_{2.5}O_4$, and $Mn_{0.75}Fe_{2.25}O_4$.

2.4. Characterization

X-ray diffraction characterization (XRD; PANalytical, X'Pert Pro, Cu-Kα 1.5406 Å) was used to determine the phase, lattice parameters, and crystal size of the samples. Investigation of the lattice parameters, crystal size, and density of $Mn_xFe_{3-x}O_4$/rGO was carried out based on the data XRD with refinement rietveld method using Rietica program. Next, identification of microscopic morphology and elemental content was used for Scanning Electron Microscopy (SEM, FEINSPECT-S50) characterization. Particle Size Analyzer (PSA, Mastersizer 3000) was used to identify the particle size of the samples. Then, to study the magnetic properties and absorption ability of the radar waves of the $Mn_xFe_{3-x}O_4$/rGO nanocomposite, Vector Network Analyzer (VNA, Advantest R3770, 8–12 GHz (X-Band)) and Permagraph (Magnet Physik Streigroever GmbH) were used to study the magnetic properties and absorption capabilities of radar waves.

3. Results and discussion

3.1. Structure of $Mn_xFe_{3-x}O_4$/r-GO nanocomposite

XRD patterns of all the samples are displayed in Figure 1. First, the data confirm the presence of only magnetite (PDF No. 19-0629) without any impurities for all samples from other study. In that study, the data of XRD supported by lattice parameter and crystal volume (Figure 2). The diffraction peaks shift to a lower angle as x increases, implying that the lattice parameter increases with Mn^{2+} incorporation [21]. Besides, the ionic radius of Mn^{2+} (0.89 Å) is larger than that of Fe^{2+} (0.77 Å) and Fe^{3+} (0.64 Å) [46]. Exactly, Mn^{2+} ions were inserted into Fe_3O_4 succesfully by replacing Fe^{2+} or Fe^{3+} ions to form $Mn_xFe_{3-x}O_4$ partially. Moreover, the lattice parameters of the $Mn_xFe_{3-x}O_4$ with x = 0.25 to 0.50 increased from 8.377 to 8.439 Å.

In this study, the structure of the $Mn_xFe_{3-x}O_4$/rGO nanocomposite was successfully characterized. The results of XRD characterization were carried out on samples of iron sand ($Mn_xFe_{3-x}O_4$), coconut shell (rGO), and $Mn_xFe_{3-x}O_4$/r-GO nanocomposites shown by RAM1 samples ($Mn_{0.25}Fe_{2.75}O_4$/rGO). The XRD $Mn_xFe_{3-x}O_4$ diffraction pattern shows that iron sand has formed a crystalline phase consisting of 93.4% magnetite (Fe_3O_4) compound and 6.6% hematite (F_2O_3) compound with a hexagonal structure with space group P63/mmc (reference code: 98-002-9041). In the rGO, the diffraction pattern consists of the main elements of carbon and oxides detected with the

chemical formula $C_{50}O_{12}H_{72}$. Based on Figure 1, the synthesized rGO sample qualitatively shows two amorphous peaks at $2\theta = 24^{o}$ (002) and 43^{o} (001) according to Acharya et al. [47] by modified Hummers method and Lavin-Lopez et al. [48] by chemical reduction, heat reduction and multiphase reduction methods. This study confirmed that coconut shell was successfully synthesized into rGO material through the solid-state reaction method.

The nanocomposite compound showed a two-phase structure consisting of $Mn_xFe_{3-x}O_4$ and rGO compounds. The diffraction pattern of the nanocomposite sample is different compared to the single-phase rGO (a) and $Mn_xFe_{3-x}O_4$ (b). Therefore, the two main phases which are $Mn_xFe_{3-x}O_4$ and rGO respectively can be identified in the diffraction pattern of the nanocomposite without the appearance of additional diffraction peaks. The $Mn_xFe_{3-x}O_4$ (a) pattern appears more than the rGO pattern (b), this is because the amount of $Mn_xFe_{3-x}O_4$ content is more than the rGO content.

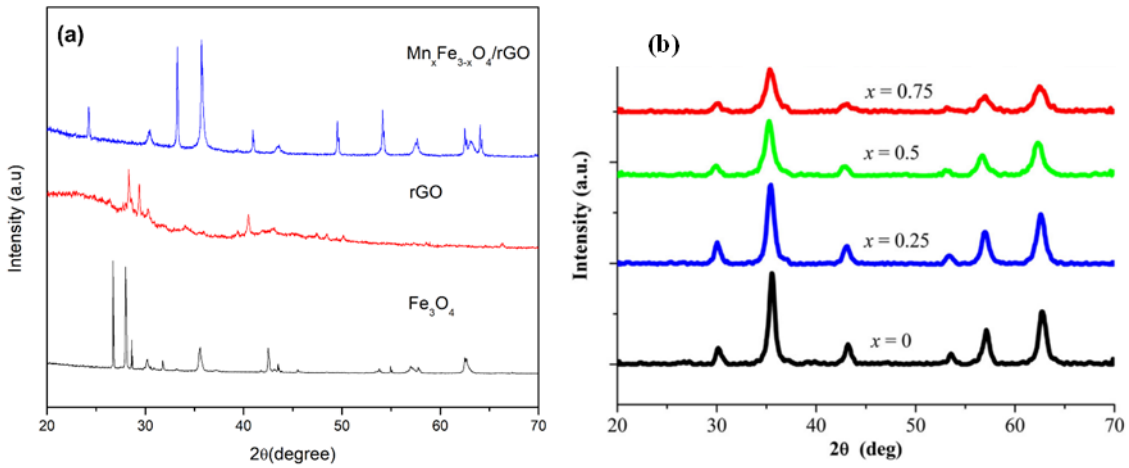

Figure 1. XRD patterns (using CuKα radiation) of the (a) Fe_3O_4, rGO, RAM1 sample ($Mn_{0.25}Fe_{2.75}O_4$/rGO) and (b) $MnxFe_{3-x}O_4$ (x = 0.25, 0.50, 0.75) (Reprinted from Ref. [21] with permission).

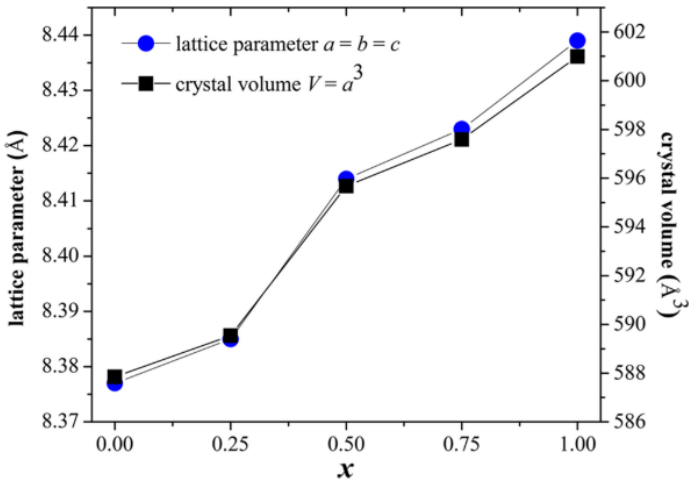

Figure 2. Lattice parameter (a) and crystal volume ($V = Å^3$) (b) of the $Mn_xFe_{3-x}O_4$ (Reprinted from Ref. [21] with permission).

For sample RAM1, the X-ray diffraction peak was identified from $Mn_xFe_{3-x}O_4$/rGO particles at 2θ = 29.9°; 35.2°; 42.9°; 53.3°; 56.6°, and 62.5° which represent Miller indices (220), (311), (400), (422), (511) and (440). The X-ray diffraction pattern of the $Mn_xFe_{3-x}O_4$/rGO nanocomposite shows a characteristic spinel ferrite structure and no other phases are formed [28,49,50]. The structural study confirms spinel structure formation with Fd3m space group for the $0 \leq x \leq 0.5$ samples. The combination with rGO did not significantly affect the shift in the X-ray diffraction pattern of $Mn_xFe_{3-x}O_4$, which has been clarified by previous studies [21,51,52]. The RAM1 sample also shows no rGO peak was found which could be caused by the XRD characterization scan (2θ angle increment) which was too fast. In another report, the disappearance of the X-ray diffraction pattern of rGO caused by the interfacial bonding of $Mn_xFe_{3-x}O_4$ with rGO resulted in a separate structure of rGO thus preventing the repetition of rGO [18]. This was also clarified by a previous study [21]. The hierarchical size of the nanocomposites was explained in detail the particle size with Particle Size Analyzer (PSA).

The sketch of the doping of Mn into Fe_3O_4 can be seen in Figure 3. The composition and cationic distributions of the $Mn_xFe_{3-x}O_4$ particles for x composition between 0 and 1 can be analyzed using the following formula in Eq 1 [53]:

$$[Mn_x^{2+}Fe_{1-x}^{3+}]_A\,[Fe_{1-x}^{2+}Fe_{1+x}^{3+}]_B\;\;O_4^{2-} \tag{1}$$

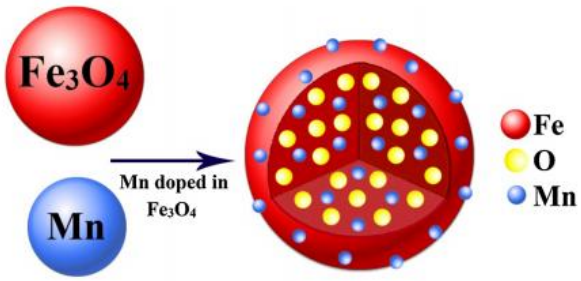

Figure 3. The sketch of the doping of Mn into Fe_3O_4.

The $Mn_xFe_{3-x}O_4$/rGO composite fabrication process was carried out using the co-precipitation method, by first doping Mn on Fe_3O_4 which was reacted with HCl to produce $FeCl_2$ and $FeCl_3$. This was carried out to get the same phase, so that the reaction can take place [54]. $Mn_xFe_{3-x}O_4$/rGO composite preparation through stoichiometric calculations has resulted in composite compounds that have been mixed with the ultrasonic method. Variations in the composition were carried out as many as 3, namely x = 0.25, x = 0.5, and x = 0.75, resulting in 3 (three) samples named consecutively as RAM1, RAM2, and RAM3. The purpose of adding Mn to Fe_3O_4 is to improve the performance of Fe_3O_4 as a radar absorbing material (RAM). In line with the research of Taufiq et al. [54]. stated that Fe_3O_4 still has a low absorption ability of radar waves. The reaction that occurs is described in Eq 2.

$$(2–x)FeCl_3 + FeCl_2 + xMnCl_2 + (8–x)NH_4OH + 4H_2O \rightarrow Mn_xFe_{3-x}O_4 + (8–x)NH_4Cl + (8–x)H_2O \tag{2}$$

The iron metal ions (Fe^{2+} and Fe^{3+}) enclosed in the square bracket represent those in the octahedral positions, while the other metal ions (Mn^{2+} and Fe^{3+}) in the round bracket represent those in the tetrahedral positions depending on the x value. Six oxygen atoms surround the metal ions in the octahedral sites, while four oxygen atoms surround the metal spinel structure can be classified

into three types: inverse, ions in the tetrahedral sites. Generally, Fe_3O_4 has an inverted spinel structure [54]. In the $Mn_xFe_{3-x}O_4$ system, the spinel, which has eight Fe^{3+} ions located in the tetrahedral mixed, and normal spinel. The systems for x = 0.25, 0.5, and 0.75 form mixed spinel structure because Mn^{2+} ions partially shift the Fe^{3+} ions in the tetrahedral positions. Physically, the $Mn_xFe_{3-x}O_4$ crystal structure modeled using the Vesta program can be seen in Figure 4 below.

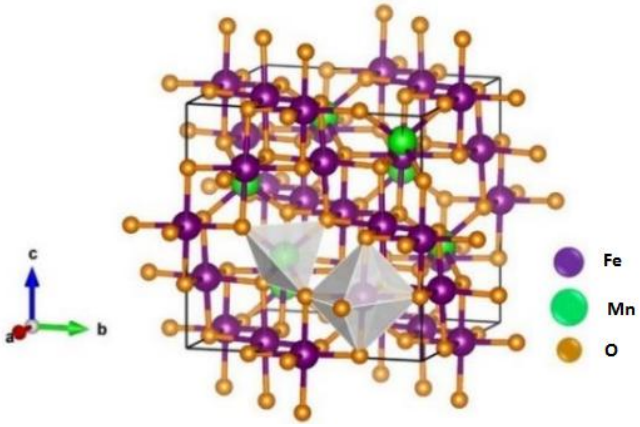

Figure 4. Crystal Structure of $Mn_xFe_{3-x}O_4$.

Figure 5 relates the rGO structure modeled using the ChemDraw program. Basically, graphene is composed of thin atoms of 2D sp^2 carbon layers that form a honeycomb-like structure. Meanwhile GO, which is a graphene derivative, contains sp^2 and sp^3 carbons and binds to a fairly high hydroxyl group (–OH) [55,56]. This is very different from rGO which has few oxygen groups and sp^3 carbon. Consequently, rGO is more similar to graphene and also has structural defects [57].

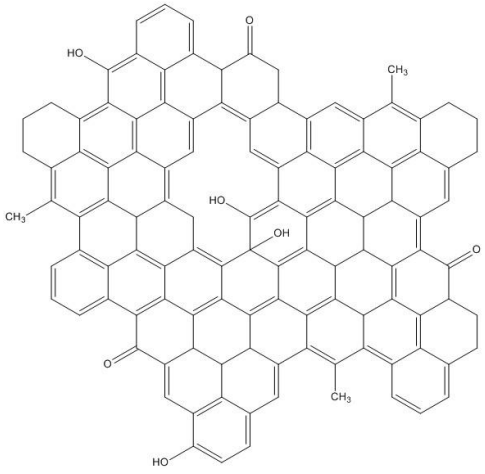

Figure 5. The Arrangement of the Atoms of rGO.

The curve of the measurement results with PSA can be seen in Figure 6. The particle size characterization of the iron sand sample that has been separated from the non-magnetic material that has been mashed and filtered shows that the raw material has a homogeneous particle size with a

single peak with an average value of 531.8 nm (Table 1). This powder was detected to be still in micro size because it still has a size of more than 100 nm. This is because there is still a coagulation process or clumping at the time of measurement, resulting in a precipitate [58]. The particle size characterization for the detected rGO samples had an average particle size of 1359 nm. This size is larger than the iron sand sample. The deposition process that occurs in rGO powder is faster than iron sand powder, so the clumping process is faster and is detected as having a larger particle size.

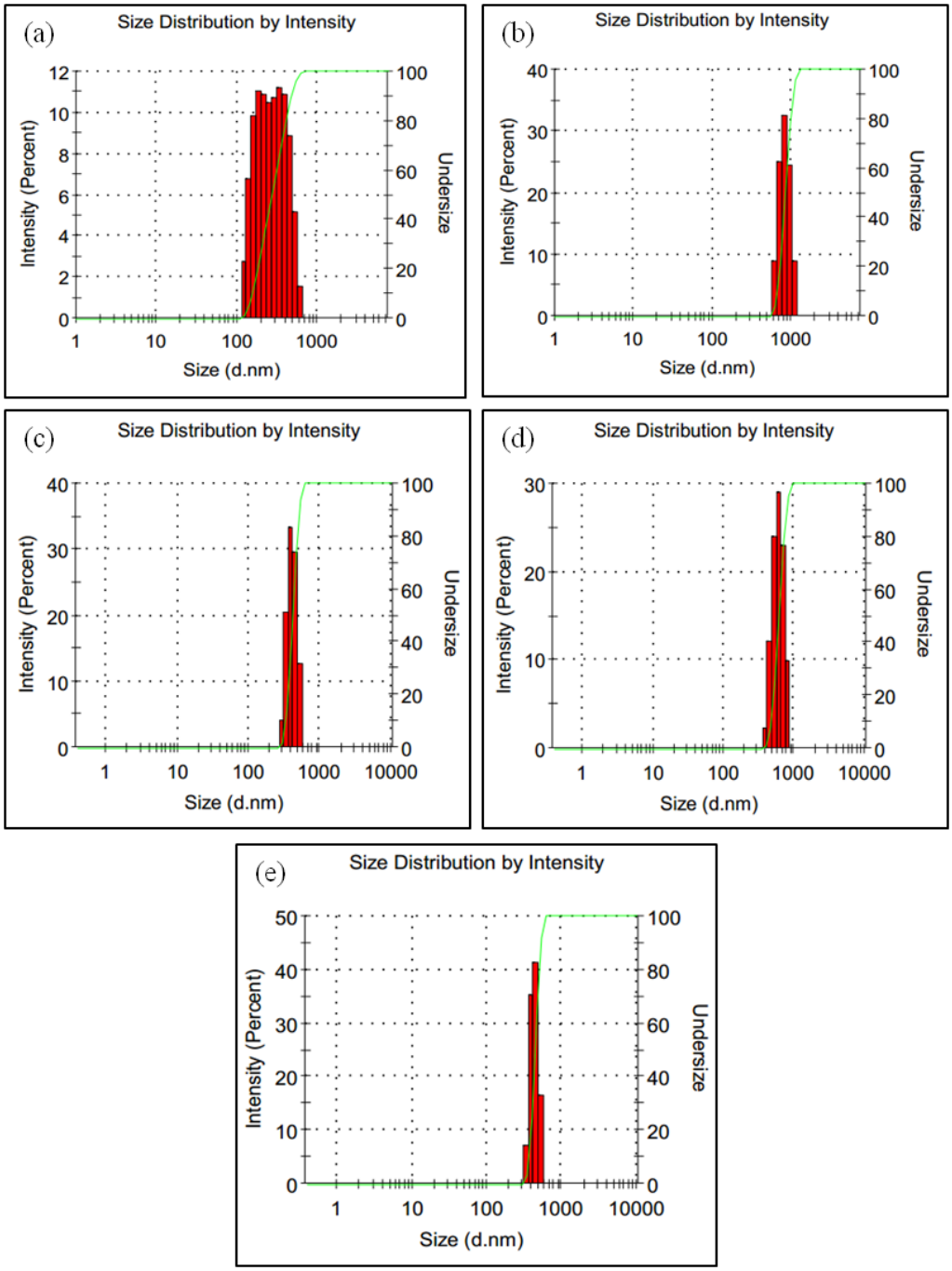

Figure 6. Size distribution by intensity of rGO (a), Fe_3O_4 (b), $Mn_xFe_{3-x}O_4$ x = 0.25 (c), $Mn_xFe_{3-x}O_4$ x = 0.5 (d), $Mn_xFe_{3-x}O_4$ x = 0.75 (e).

Table 1. Distribution results of samples.

Samples	Distribution results				Z-Avg (nm)
	Size (d.nm)	% Int	σ	%Pd	
Fe_3O_4	369.3	53.3	93.00	25.2	531.8
	194.8	46.7	41.21	21.2	
rGO	835.0	100.0	134.9	16.2	1359
$Mn_{0.25}Fe_{2.75}O_4$	416.8	100.0	63.62	15.3	1049
$Mn_{0.5}Fe_{2.5}O_4$	613.9	100.0	110.5	18.0	1432
$Mn_{0.75}Fe_{2.25}O_4$	440.4	100.0	53.65	12.2	1531

In general, the addition of the composition of Mn and rGO to Fe_3O_4 nanoparticles causes the crystallinity level of Fe_3O_4 to increase teorically [12]. This is proven in Figure 6 which shows that the distribution peaks of $Mn_xFe_3O_4$/rGO in nanocomposites (x = 0.25 to x = 0.75) appear sharper when compared to pure Fe_3O_4. The increase in Mn composition in $Mn_xFe_{3-x}O_4$/rGO nanocomposites results in an increase in the intensity of the $Mn_xFe_{3-x}O_4$/rGO peak except for x = 0.75 which is lower when compared to x = 0.5. This is because the x = 0.75 particle distribution is lower than other nanocomposites of particle sizes (440.4 nm), but the average of particle size from x = 0.25 to x = 0.75 increase. The increase in particle size is caused by the large number of Mn particles that push Fe. Theoretically, the size of Fe^{2+} and Fe^{3+} ions is larger than that of Mn^{2+} ions. However, when the number of Mn^{2+} ions is more pressing the Fe^{2+} ions will result in clumping, resulting in a larger particle size than before being pushed by Mn^{2+}. This phenomenon is theoretically reinforced that in the voltaic series, Mn is to the left of Fe, so it has more reactive properties and is stronger against Fe. The more Mn metal ions push Fe from Fe_3O_4, the larger the particle size of the $Mn_xFe_{3-x}O_4$ nanocomposite. This is also confirmed in Table 1 which shows the particle size of the sample.

Uniquely, the Fe_3O_4 available in this work did not produce polymorphs. Polymorphs that are often produced in the synthesis of Fe_3O_4, like α-Fe_2O_3, γ-Fe_2O_3, dan α-Fe_3O_4 [59]. This is because the synthesized Fe_3O_4 comes from natural iron sand. Natural iron sand contains stable Fe_2O_3, so it does not cause porosity which causes Fe_2O_3 variations in Fe_3O_4 synthesis [54].

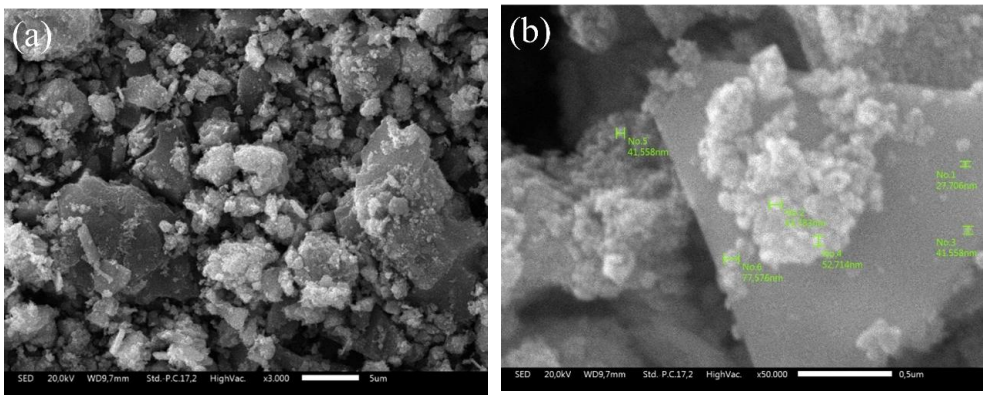

Figure 7. SEM images of $Mn_{0.5}Fe_{2.5}O_4$/rGO with (a) 3000 and (b) 50,000 magnification with the particle size.

The SEM images of $Mn_xFe_{3-x}O_4$/rGO nanocomposites with Mn doping composition of x = 0.5

is shown in Figure 7. As shown in Figure 7a, the morphology of the nanocomposites consists of 3 particle shapes namely spheres, chunks, and worm-like structures. Sequentially, these shapes describe the Fe_3O_4 nanoparticles, Mn [60,61], and rGO [62]. Qualitatively, it is observed that the sphere of Fe_3O_4 tends to agglomerate. The size of Fe_3O_4 nanoparticles is smaller than that of Mn which has relatively irregular chunks. In addition, the Mn surface also shows some agglomeration of Fe_3O_4, while rGO fills the gap between Fe_3O_4 and Mn [63]. Illustrated in Figure 5, rGO is a carbon material that is activated with acids to form OH-functional groups, so that the rGO will bind to the positive charge of Fe_3O_4 which causes the Fe_3O_4 to fill the surface of the carbon material. Based on Figure 5a, few rGO surfaces are covered by agglomeration of Fe_3O_4. This is because the density of Fe_3O_4 is higher than that of rGO [64]. Figure 5b indicates the morphology of Mn-doped Fe_3O_4 nanoparticles with a magnification of 50,000 and shows that the Fe_3O_4 and Mn nanoparticles are evenly dispersed on the rGO surface. Furthermore, the EDX results show that the composition of heavy elements C, O, and Fe are 28.72, 36.17, and 27.78% and another is Mn, respectively, which confirms the presence of Fe_3O_4 nanoparticles, rGO, and Mn that form $Mn_xFe_{3-x}O_4$ composites. The presence of Fe_3O_4 was confirmed by the presence of Fe and O elements. Meanwhile, the rGO were confirmed by the presence of element C, and doping of Mn were confirmed by the presence of element Mn.

3.2. The magnetic properties of $Mn_xFe_{3-x}O_4$/rGO

Magnetic properties in the form of hysteresis loops for $Mn_xFe_{3-x}O_4$/rGO nanocomposite samples can be seen in Figure 8. All curves show the characteristics of soft and tall soft magnetic hysteresis loops.

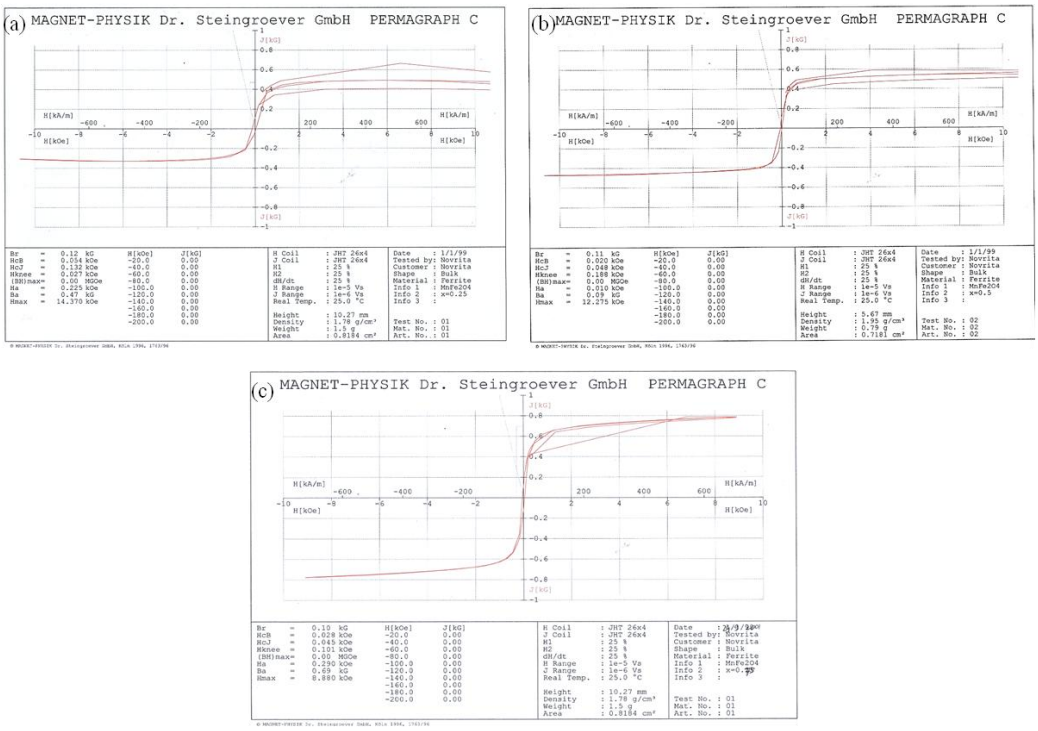

Figure 8. Hysteresis loops of MnxFe$_{3-x}$O$_4$/r-GO with (a) x = 0.25, (b) x = 0.50, and (c) x = 0.75.

A summary of the magnetic properties that obtained in this research, can be seen in Table 2.

Table 2. Magnetic properties of $Mn_xFe_{3-x}O_4$/rGO.

Samples	Br (kG)	H_cJ (kOe)	H_{max} (kOe)
$Mn_{0.25}Fe_{2.75}O_4$	0.12	0.132	14.370
$Mn_{0.5}Fe_{2.5}O_4$	0.11	0.048	12.275
$Mn_{0.75}Fe_{2.25}O_4$	0.10	0.045	8.880

The sample of $Mn_{0.25}Fe_{2.75}O_4$ had the highest remanent induction (Br), coercivity (H_cJ), and the highest magnetic field strength (H_{max}) compared to the other samples, 0.12 kg, 0.132 kOe, and 14.370 kOe, respectively. The results of this characterization indicate that the effect of composition affects the magnetic properties. The addition of Mn elements reduces the values of Br, H_cJ, and H_{max}. Theoretically, Fe has higher magnetic properties than Mn. Thus, when more Mn replaces Fe, the magnetic properties will decrease. However, it must be analyzed further through the results of the reflection loss of the synthesized sample.

3.3. Reflection loss of $Mn_xFe_{3-x}O_4$/rGO

Reflection loss is a characteristic that shows the ability of radar wave absorption from $Mn_xFe_{3-x}O_4$/rGO. Reflection loss of each sample has been characterized using VNA with the results of the reflection loss and frequency curves as shown in Figure 9. The results show that there has been absorption of electromagnetic waves in the frequency range between 7–13 GHz with the absorption frequency range at 2–14 GHz. At this frequency, it shows that the $Mn_xFe_{3-x}O_4$/r-GO nanocomposite can be applied as a RAM material in the X-Band 8–12 GHz frequency range. Figure 9 shows RL of the $Mn_xFe_{3-x}O_4$/rGO nanocomposites at a frequency of 8–12 GHz which were calculated by using Eqs 3 and 4.

$$RL = 20\log\frac{|Z_{in}-Z_0|}{|Z_{in}+Z_0|} \tag{3}$$

Z_{in} value was calculated by using Eq 3 below.

$$Z_{in} = Z_0\ \sqrt{\mu_r\varepsilon_r}\ \tanh\left[j\,\frac{2\pi f d}{c}\sqrt{\mu_r\varepsilon_r}\right] \tag{4}$$

where Z_{in} and Z_{in} are input and output impedance values. While μ_r and $\mathcal{E}_r$ are the permeability and complex permittivity of the material, c represents the velocity of the radar in a vacuum, f is the frequency of radar, and d is the thickness of the material when tested [65].

In Figure 9 for the sample of $Mn_{0.25}Fe_{2.75}O_4$/rGO nanocomposite, absorption of electromagnetic waves has occurred in the frequency range between 8.9–11.5 GHz with the absorption peak frequency at 11.5 GHz of −11.8 dB with a thickness of 1.5 mm adsorption field. Likewise for the $Mn_{0.5}Fe_{2.5}O_4$/rGO nanocomposite sample, absorption occurs in the frequency range between 9–11.3 GHz with the absorption peak frequency at 11.3 GHz of −11.5 dB. Meanwhile, for the $Mn_{0.75}Fe_{2.25}O_4$/r-GO nanocomposite sample, absorption has occurred in the frequency range between 8.8–11.5 GHz with the absorption peak frequency at 11.5 GHz of −1.95 dB.

Fe_3O_4 has an *RL* of −5.58 dB at a frequency of 10.58 GHz. The low *RL* value owned by Fe_3O_4 is

due to the fact that this sample only consists of magnetic material, thus RAM only absorbs the magnetic part of the radar. In this study, the increase in radar absorption is increased by adding Fe_3O_4 with rGO materials. That is because rGO belongs to good dielectric material. Based on Figure 9, it is noticed that the absorption capability of radar from $Mn_xFe_{3-x}O_4$/rGO nanocomposites is stronger than that of Fe_3O_4 nanoparticles. This indicates that the absorption properties of radar increase if added by rGO materials. Physically, this phenomenon occurs since the absorption of radar from Fe_3O_4 nanoparticles only comes from natural resonance and domain wall resonance, so that with the addition of rGO, the dielectric loss properties of the rGO is introduced and the interface polarization between Fe_3O_4 and rGO is introduced. In detail, the *RL* values of nanocomposites are shown in Table 3. Based on Table 3, it can be seen that the *RL* values of the $Mn_xFe_{3-x}O_4$/rGO nanocomposites are higher than those of MWCNT/Fe_3O_4 [66] and $ZnFe_2O_4$ [67]. The addition of dielectric material also causes the absorption bandwidth of the $Mn_xFe_{3-x}O_4$/rGO nanocomposites to widen. Differences in composition affect the absorption of $Mn_xFe_{3-x}O_4$/rGO nanocomposite RAM material. At composition x = 0.75 is the highest absorption with −11.95 dB.

Generally, the $Mn_xFe_{3-x}O_4$ material in RAM applications acts as a magnetic material. Based on Table 3, the single material is not optimal in absorbing radar waves. Fe_3O_4 material obtained a low RL value of −5 dB [68]. The $Mn_{0.75}Fe_{2.25}O_4$/rGO material was able to increase the RL value to −6.95 dB compared to pure Fe_3O_4 [17]. This is due to the presence of Mn^{2+} ions which can increase the polarization of the space charge [69]. The ability of magnetic loss in $Mn_xFe_{3-x}O_4$ material occurs when the direction of the magnetic moment which is relatively antiparallel in the tetrahedral and octahedral regions will be rectified [19]. Generally, $Mn_xFe_{3-x}O_4$ materials can produce magnetic loss consisting of eddy current loss and natural resonance loss [30]. Furthermore, the magnetic loss capability is more dominant due to the eddy current loss phenomenon, as expressed in Eq 5 [28].

$$C_0 = \mu'' (\mu')^{-2} f^{-1} \quad (5)$$

With C_0 as the value representing the eddy current loss. If depicted in a graph C_0 with f, then the eddy current loss is indicated by a constant value of C_0. In the study of Tajik et al., the $Mn_xFe_{3-x}O_4$ material showed a constant C_0 value at frequencies above 8 GHz [70]. In another report, Modaresi et al. reported the same [28]. Conversely, if the value of C_0 is not constant, it can be indicated that there is a natural resonance loss phenomenon from the magnetic material. The relatively small crystal size has the potential to increase the RL value, which is caused by the exchange length resonance of the magnetic energy of a material [55]. Thus, the $Mn_xFe_{3-x}O_4$ material can be used as a potential magnetic material in RAM applications.

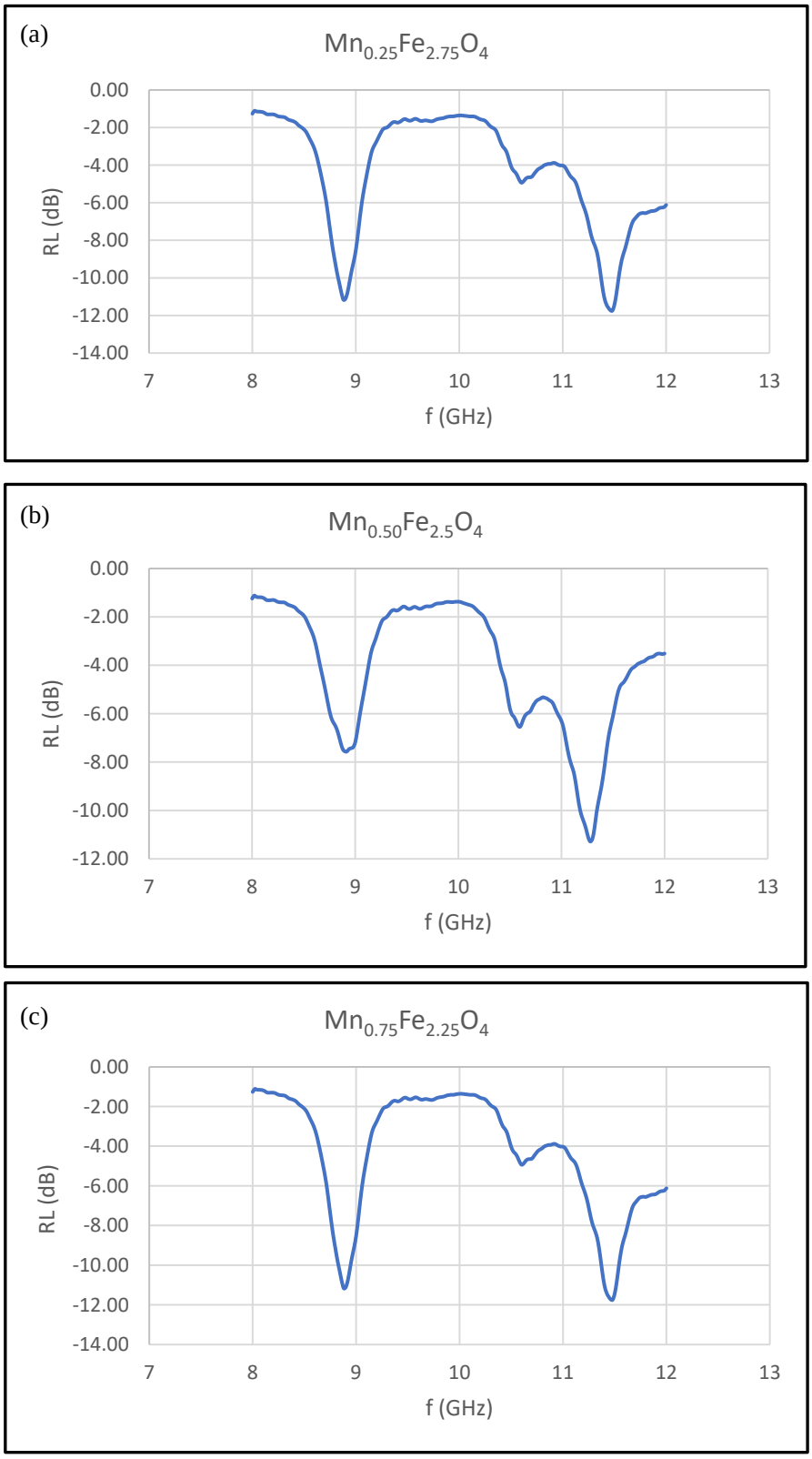

Figure 9. Reflection loss of the $Mn_xFe_{3-x}O_4$/rGO nanocomposites with (a) x = 0.25, (b) x = 0.50, (c) x = 0.75.

Table 3. *RL* value of the $Mn_xFe_{3-x}O_4$/rGO nanocomposites.

Samples	RL (dB)	Ref.
$Mn_{0.25}Fe_{2.75}O_4$/rGO	−11.8	-
$Mn_{0.5}Fe_{2.5}O_4$/rGO	−11.5	-
$Mn_{0.75}Fe_{2.25}O_4$/rGO	−11.95	-
rGO	−5	[52]
rGO	−3.3	[37]
Fe_3O_4	−3.3	[66]
Fe_3O_4	−5	[68]
$ZnFe_2O_4$	−10.0	[67]
MWCNT/Fe_3O_4	−10.0	[66]

Furthermore, rGO is a unique material, which refers to its special characteristic which is it can produce dielectric loss. In the report of Liu et al., dielectric materials depend on the phenomenon of dipole and electron polarization [37]. Inside an atom, the influence of the electric field from electromagnetic waves will cause electron polarization. If viewed at the molecular level, each molecule has a dipole moment, which when applied by an external electric field will form a charge separation or dipole polarization. In the rGO system, dipole polarization occurs in the structural defects and the presence of various functional groups [71]. For example, Qiao et al. representing the interaction of electromagnetic waves with the structural defects of rGO, will result in an asymmetric charge distribution to form a dipole formation [72]. This causes the dipole to continue to rotate in electromagnetic waves, which in turn converts electromagnetic wave energy into heat energy [73]. In fact, electrons on the surface of rGO can interact with electromagnetic wave energy [74]. Consequently, the electrons will migrate and collide with the rGO lattice, where the energy of the electromagnetic waves is converted into heat energy [73]. Debye's dipolar relaxation theory is usually used to confirm the ability of dielectric loss, as expressed in Eq 6 [28].

$$\varepsilon' - (\varepsilon_s + \varepsilon_\infty/2)^2 + (\varepsilon'')^2 = (\varepsilon_s - \varepsilon_\infty/2)^2 \quad (6)$$

Where ε_s and ε_∞ are static permittivity and relative dielectric permittivity. If and are expressed as x and y axes, a semi-circular Cole-Cole graph is formed. According to Chai and colleagues, the presence of a semi-circle pattern indicates a relaxation process, which is caused by the absorption of the electric field from electromagnetic waves [67]. Furthermore, Shu et al. reported that the distortion of the semi-circular Cole-Cole graph in the rGO material indicates the presence of polarization [74]. Furthermore, based on the previous SEM image of the composite sample in Figure 7, rGO forms cavities and is filled with $Mn_xFe_{3-x}O_4$ particles. The presence of cavities in rGO has the potential to increase the value of reflection loss, which is caused by electromagnetic waves undergoing multiple reflections [75]. Thus, the rGO material has potential in RAM applications. Although, based on Table 3, the reflection loss value of rGO is still low at −5 dB, so it is necessary to combine it with magnetic materials.

$Mn_xFe_{3-x}O_4$ deposition strategy on the surface of rGO is one of the appropriate ways to produce microcurrent networks [76]. The mechanism, $Mn_xFe_{3-x}O_4$ acts as an electron-hopping bridge between adjacent rGO layers [55]. More deeply, electron-hopping is expressed as contact conductivity ($\sigma_{contact}$) as a function of temperature (T) as in Eq 7 [76].

$$\sigma_{contact}\,(T) = K_h/T \exp(-U/k_BT) \quad (7)$$

Where K_h is the prefactor, U is the barrier potential and k_B is the Boltzmann constant. As the equation above, conductivity is caused by electron-hopping followed by an increase in temperature. The micro current network that is formed will produce a conduction loss [55]. The phenomenon of conduction loss is characterized by a decrease in the permittivity value as the frequency increases, which is useful for weakening the energy of electromagnetic waves. However, Cao and colleagues reported that the phenomenon of relaxation or an increase in temperature that is too high causes a conductivity network not to form [71]. Consequently, at high frequencies, the dielectric loss capability will decrease. One solution is to adjust the mass composition of rGO with $Mn_xFe_{3-x}O_4$. In addition, the presence of interfacial interactions between $Mn_xFe_{3-x}O_4$ and rGO has the potential to produce interfacial polarization [13]. Physically, the interface interaction accumulates the migration and diffusion of the carrier so as to form a spatial separation consisting of positive and negative charges [77]. Consequently, between the boundaries of the $Mn_xFe_{3-x}O_4$ and rGO materials, a balance formation is formed in the form of a region of spatial charges and an electric field. However, changing the direction of the electromagnetic wave field can change the charge pattern so that the electromagnetic wave energy will be dissipated [78]. Interfacial polarization can also be identified through Debye's dipolar relaxation theory as studied above.

According to Table 3, the $Mn_xFe_{3-x}O_4$/rGO composite of the three variations showed fantastic results, namely higher reflection loss values than the single material. The combination of magnetic and dielectric materials provides a synergy effect with good impedance match results (Z ~ 1) [79]. Furthermore, this composite system contains a magnetic material, this is in accordance with the results of the reflection loss value obtained from the tests that have been carried out.

Based on the results of the previous research, it was shown that, if the *RL* value obtained <−15 dB, it indicates that if 96.9% of the radar waves are absorbed by the nanocomposite. Meanwhile, if the RL value obtained <−20 dB, then the absorbed wave is almost 99.0% [80]. In this research, the RL value of nanocomposites has a range between −2 to −14 dB or <−20 dB. Thus, it can be concluded that the waves absorbed by nanocomposites in this study are around 96.9–99.0%. Two main aspects affecting the increase of radar absorption by $Mn_xFe_{3-x}O_4$/rGO nanocomposites in this study are first, the efficient complementarity between dielectric loss and magnetic loss which is indicated by the relative permittivity and permeability values must be fulfilled [68,81]. If Fe_3O_4 nanoparticles stand alone as a compiler of RAM, it can be construed that the resulting *RL* value is still low. This is due to the large disparity between permeability and permittivity which interferes with impedance matching. Thus, in the $Mn_xFe_{3-x}O_4$/rGO system, the Fe_3O_4 nanoparticles act as absorbents of the magnetic parts, and rGO, is as dielectric absorbers of incoming radar. Besides, the rGO also acts as a nucleation site for Fe_3O_4 which prevents or reduces the aggregation of these nanoparticles. Second, there is interfacial polarization between Fe_3O_4-rGO, where multi-interfaces on nanocomposites will produce significant polarization interfaces that will increase the value of dielectric loss at high frequencies [65]. This is indicated when the addition of rGO absorption material occurs at a frequency of around 11 GHz. Thus, the development of $Mn_xFe_{3-x}O_4$/rGO nanocomposites in this research provides new opportunities for large-scale development for the application of high-performance microwave absorbing materials based on local natural materials through environmentally friendly synthesis.

3.4. Practical implication and outlook

Uniquely, in this study, reduced-graphene oxide (rGO) synthesized from coconut shell waste has the potential to be developed as a dielectric material from RAM. This is relevant to the data presented in Table 3 that rGO can absorb electromagnetic waves of −5 dB [52] added with the findings from this study which combines natural materials of natural iron sand and coconut shell waste, it produces an RL value of −11.95 dB. In general, coconut shell waste is very easy to obtain from the community, especially in Indonesia. Theorically, coconut shell has a high cellulose content, so it contains a high carbon content as well [82,83]. Carbon has the ability to absorb electromagnetic waves, so it has the potential to be developed as a dielectric material. Further research on the use of natural materials can be developed towards extracting the potential of the material itself. Natural iron sand can be extracted as a source of Fe_2O_3 which can be synthesized into Fe_3O_4 with benefits as an environmentally friendly magnetic material [84], antimicrobial [69], and anti-cancer agent [79]. Meanwhile, coconut shell waste can be synthesized into rGO with the benefit of being a dielectric material for Radar Absorbing Material (RAM) [56], corrosion protection [85], and electrochemical sensor [70].

4. Conclusions

The $Mn_xFe_{3-x}O_4$/rGO nanocomposites were successfully synthesized by using an environmental precipitation method. Meanwhile, with the addition of rGO in the $Mn_xFe_{3-x}O_4$/rGO nanocomposites, their *RL* increases significantly because the nanocomposites consist of magnetic loss and dielectric loss which increases the radar absorption. Interestingly, the *RL* value of the $Mn_xFe_{3-x}O_4$/rGO nanocomposites ranges from −2.0 to −14.0 dB which shows their radar absorption capability is in the range of 96.9%–99.0%.

Acknowledgments

This work was supported by Faculty of Mathematics and Natural Sciences, Universitas Negeri Malang. The writer was inspired by the special people, like KH. Muhammad Zaini Abdul Ghani, Prof. Effendy, Ph.D, and Prof. Hadi Nur, Ph.D. Special thanks to my best close friend, Muhammad Roy Asrori, S.Pd.

Conflict of Interest

The authors stated that there is no conflict of interest.

References

1. Dayo ZA, Cao Q, Wang Y (2020) A compact high-gain coplanar waveguide-fed antenna for military RADAR applications. *Int J Antennas Propag* 2020: 8024101. https://doi.org/10.1155/2020/8024101
2. Wen F (2019) Direction finding in MIMO radar with large antenna arrays and nonorthogonal waveforms. *Digit Signal Process* 94: 75–83. https://doi.org/10.1016/j.dsp.2019.06.008

3. Wagner T, Feger R, Stelzer A (2017) Radar signal processing for jointly estimating tracks and micro-doppler signatures. *IEEE Access* 5: 1220–1238. https://doi.org/10.1109/ACCESS.2017.2667720
4. Bandara P, Carpenter DO (2018) Planetary electromagnetic pollution: it is time to assess its impact. *Lancet Planet Health* 2: e512–e514. https://doi.org/10.1016/S2542-5196(18)30221-3
5. Miah T, Kamat D (2017) Current understanding of the health effects of electromagnetic fields. *Pediatr Ann* 46: e172–e174. https://doi.org/10.3928/19382359-20170316-01
6. Sabath F (2017) A systematic approach for electromagnetic interference risk management. *IEEE EMC* 6: 99–106. https://doi.org/10.1109/MEMC.0.8272296
7. Mas'udah KW, Hendy, Taufiq A (2020) Characteristics of crystal structure and microwave absorption of silica particles as the effect of sintering temperature. *AIP Conf Proc* 2231: 040072. https://doi.org/10.1063/5.0002477
8. Hardianto YP, Taufiq A, Hidayat A, et al. (2018) Nanostructure analysis for microwave absorption properties of Fe_3O_4 particles by symmetry top rotational molecular model. *IOP Conf Ser-Mater Sci Eng* 367: 012009. https://doi.org/10.1088/1757-899X/367/1/012009
9. Atay HY (2017) Multi-functional materials for military aircrafts; radar absorbing and flame retardant composites. *RESM* 3: 45–54. http://dx.doi.org/10.17515/resm2016.38ma0204
10. Feng J, Zong Y, Sun Y, et al. (2018) Optimization of porous $FeNi_3$/N-GN composites with superior microwave absorption performance. *Chem Eng J* 345: 441–451. https://doi.org/10.1016/j.cej.2018.04.006
11. Taufiq A, Bahtiar S, Saputro RE, et al. (2020) Fabrication of $Mn_{1-x}Zn_xFe_2O_4$ ferrofluids from natural sand for magnetic sensors and radar absorbing materials. *Heliyon* 6: e04577. https://doi.org/10.1016/j.heliyon.2020.e04577
12. Taufiq A, Sutiami R, Subadra SU, et al. (2020) Radar absorption performance of Fe_3O_4/AC/PANI nanocomposites prepared from natural iron sand. *Int J Eng* 33: 304–313. https://doi.org/10.5829/ije.2020.33.02b.15
13. Li F, Zhuang L, Zhan W, et al. (2020) Desirable microwave absorption performance of $ZnFe_2O_4$@ZnO@rGO nanocomposites based on controllable permittivity and permeability. *Ceram Int* 46: 21744–21751. https://doi.org/10.1016/j.ceramint.2020.05.283
14. Andreev VG, Menshova SB, Klimov AN, et al. (2015) The influence of basic composition and microstructures on the properties of Ni-Zn ferrite radio-absorbing materials. *J Magn Magn Mater* 393: 569–573. https://doi.org/10.1016/j.jmmm.2015.06.030
15. Sano E, Akiba E (2014) Electromagnetic absorbing materials using nonwoven fabrics coated with multi-walled carbon nanotubes. *Carbon* 78: 463–468. https://doi.org/10.1016/j.carbon.2014.07.027
16. Wei S, Yan R, Shi B, et al. (2019) Characterization of flexible radar-absorbing materials based on ferromagnetic nickel micron-fibers. *J Ind Text* 49: 58–70. https://doi.org/10.1177/1528083718772304
17. Rahmawati R, Melati A, Taufiq A, et al. (2017) Preparation of MWCNT-Fe_3O_4 nanocomposites from iron sand using sonochemical route. *IOP Conf Ser-Mater Sci Eng* 202: 012013. https://doi.org/10.1088/1757-899X/202/1/012013
18. Sui M, Fu T, Sun X, et al. (2018) Unary and binary doping effect of M^{2+} (M = Mn, Co, Ni, Zn) substituted hollow Fe_3O_4 approach for enhancing microwave attenuation. *Ceram Int* 44: 17138–17146. https://doi.org/10.1016/j.ceramint.2018.06.167

19. Tian C, Du Y, Cui C, et al. (2017) Synthesis and microwave absorption enhancement of yolk-shell Fe_3O_4@C microspheres. *J Mater Sci* 52: 6349–6361. https://doi.org/10.1007/s10853-017-0866-3
20. Jian X, Wu B, Wei Y, et al. (2016) Facile synthesis of Fe_3O_4/GCs composites and their enhanced microwave absorption properties. *ACS Appl Mater Interfaces* 8: 6101–6109. https://doi.org/10.1021/acsami.6b00388
21. Taufiq A, Giri E, Putra R, et al. (2015) Nanoscale clustering and magnetic properties of $Mn_xFe_{3-x}O_4$ particles prepared from natural magnetite. *J Supercond Nov Magn* 28: 2855–2863. https://doi.org/10.1007/s10948-015-3111-9
22. Sunaryono S, Hidayat MF, Mufti N, et al. (2020) The effect of Mn doping on nano structure and magnetic properties of $Mn_xFe_{3-x}O_4$-PEG/PVP/PVA based ferrogel. *J Polym Res* 27: 1–10. https://doi.org/10.1007/s10965-020-02065-w
23. Vamvakidis K, Katsikini M, Vourlias G, et al. (2015) Composition and hydrophilicity control of Mn-doped ferrite ($Mn_xFe_{3-x}O_4$) nanoparticles induced by polyol differentiation. *Dalt Trans* 44: 5396–5406. https://doi.org/10.1039/C5DT00212E
24. Jouyandeh M, Ganjali MR, Seidi F, et al. (2020) Nonisothermal cure kinetics of epoxy/polyvinylpyrrolidone functionalized superparamagnetic nano-Fe_3O_4 composites: Effect of Zn and Mn doping. *J Compos Sci* 4: 55. https://doi.org/10.3390/jcs4020055
25. Mohanty D, Mallick P, Biswal SK, et al. (2020) Investigation of structural, dielectric and electrical properties of $ZnFe_2O_4$ composite. *Mater Today Proc* 33: 4971–4975. https://doi.org/10.1016/j.matpr.2020.02.827
26. Saha P, Rakshit R, Mandal K (2019) Enhanced magnetic properties of Zn doped Fe_3O_4 nano hollow spheres for better bio-medical applications. *J Magn Magn Mater* 475: 130–136. https://doi.org/10.1016/j.jmmm.2018.11.061
27. Zhang Y, Wu Y, Qin Q, et al. (2016) A study of the mechanism of microwave-assisted ball milling preparing $ZnFe_2O_4$. *J Magn Magn Mater* 409: 6-9. https://doi.org/10.1016/j.jmmm.2016.02.066
28. Modaresi N, Afzalzadeh R, Aslibeiki B, et al. (2017) Competition between the impact of cation distribution and crystallite size on properties of $Mn_xFe_{3-x}O_4$ nanoparticles synthesized at room temperature. *Ceram Int* 43: 15381-15391. https://doi.org/10.1016/j.ceramint.2017.08.079
29. Taufiq A, Yuliantika D, Sunaryono S, et al. (2018) Nanopowder and magnetic fluid synthesis of $Zn_{0.2}Fe_{2.8}O_4$ particles and their structural and magnetic behaviors. *J Phys-Conf Ser* 1091: 012030. https://doi.org/10.1088/1742-6596/1091/1/012030
30. Daoush WM (2017) Co-Precipitation and magnetic properties of magnetite nanoparticles for potential biomedical applications. *J Nanomedicine Res* 5: 00118. https://doi.org/10.15406/jnmr.2017.05.00118
31. Taufiq A, Bahtiar S, Hidayat N, et al. (2017) Preparation of superparamagnetic $Zn_{0.5}Mn_{0.5}Fe_2O_4$ particle by coprecipitation-sonochemical method for radar absorbing material. *IOP Conf Ser-Mater Sci Eng* 202: 012024. https://doi.org/10.1088/1757-899X/202/1/012024
32. Rahmawati R, Taufiq A, Sunaryono S, et al. (2018) Synthesis of magnetite (Fe_3O_4) nanoparticles from Iron sands by coprecipitation-ultrasonic irradiation methods. *J Mater Environ Sci* 9: 155–160. https://doi.org/10.26872/jmes.2018.9.1.19

33. Sunaryono, Taufiq A, Mashuri, et al. (2015) Various magnetic properties of magnetite nanoparticles synthesized from iron-sands by coprecipitation method at room temperature. *Mater Sci Forum* 827: 229–234. https://doi.org/10.4028/www.scientific.net/MSF.827.229
34. Jouyandeh M, Paran SMR, Khadem SSM, et al. (2020) Nonisothermal cure kinetics of epoxy/$Mn_xFe_{3-x}O_4$ nanocomposites. *Prog Org Coatings* 140: 105505. https://doi.org/10.1016/j.porgcoat.2019.105505
35. Li M, Gao Q, Wang T, et al. (2016) Solvothermal synthesis of $Mn_xFe_{3-x}O_4$ nanoparticles with interesting physicochemical characteristics and good catalytic degradation activity. *JMADE* 97: 341–348. https://doi.org/10.1016/j.matdes.2016.02.103
36. Luo J, Shen P, Yao W, et al. (2016) Synthesis, characterization, and microwave absorption properties of reduced graphene oxide/strontium ferrite/polyaniline nanocomposites. *Nanoscale Res Lett* 11: 141. https://doi.org/10.1186/s11671-016-1340-x
37. Liu P, Yao Z, Zhou J (2016) Fabrication and microwave absorption of reduced graphene oxide/$Ni_{0.4}Zn_{0.4}Co_{0.2}Fe_2O_4$ nanocomposites. *Ceram Int* 42: 9241–9249. https://doi.org/10.1016/j.ceramint.2016.03.026
38. Saeed MS, Seyed-yazdi J, Hekmatara H (2020) Fe_2O_3/Fe_3O_4/PANI/MWCNT nanocomposite with the optimum amount and uniform orientation of Fe_2O_3/Fe_3O_4 NPs in polyaniline for high microwave absorbing performance. *J Alloys Compd* 843: 156052. https://doi.org/10.1016/j.jallcom.2020.156052
39. Zhao C, Shen M, Li Z, et al. (2016) Green synthesis and enhanced microwave absorption property of reduced graphene oxide-$SrFe_{12}O_{19}$ nanocomposites. *J Alloys Compd* 689: 1037–1043. https://doi.org/10.1016/j.jallcom.2016.08.078
40. Wang X, Zhang B, Zhang W, et al. (2017) Super-light Cu@Ni nanowires/graphene oxide composites for significantly enhanced microwave absorption performance. *Sci Rep* 7: 1–13. https://doi.org/10.1038/s41598-017-01529-2
41. Luo J, Zuo Y, Shen P, et al. (2017) Excellent microwave absorption properties by tuned electromagnetic parameters in polyaniline-coated $Ba_{0.9}La_{0.1}Fe_{11.9}Ni_{0.1}O_{19}$/reduced graphene oxide nanocomposites. *RSC Ad*v 7: 36433–36443. https://doi.org/10.1039/C7RA06800J
42. Ma J, Wang X, Cao W, et al. (2018) A facile fabrication and highly tunable microwave absorption of 3D flower-like Co_3O_4-rGO hybrid-architectures. *Chem Eng J* 339: 487–498. https://doi.org/10.1016/j.cej.2018.01.152
43. Wardhani MK, Astuti F, Darminto D (2016) Study on physical properties of reduced graphene oxide from heating coconut shell. *JPSE* 1: 1–6. https://doi.org/10.17977/um024v1i12016p001
44. Ogino I, Fukazawa G, Kamatari S, et al. (2018) The critical role of bulk density of graphene oxide in tuning its defect concentration through microwave-driven annealing. *J Energy Chem* 27: 1468–1474. https://doi.org/10.1016/j.jechem.2017.09.010
45. Shu R, Li W, Zhou X, et al. (2018) Facile preparation and microwave absorption properties of RGO/MWCNTs/$ZnFe_2O_4$ hybrid nanocomposites. *J Alloys Compd* 743: 163–174. https://doi.org/10.1016/j.jallcom.2018.02.016
46. Li HY, Kouh T, Shim IB, et al. (2012) Investigation of cation distribution in single crystalline $Fe_{3-x}Mn_xO_4$ microspheres based on Mössbauer spectroscopy. *J Appl Phys* 111: 07B544. https://doi.org/10.1063/1.3687007

47. Acharya S, Alegaonkar P, Datar S (2019) Effect of formation of heterostructure of $SrAl_4Fe_8O_{19}$/RGO/PVDF on the microwave absorption properties of the composite. *Chem Eng J* 374: 144–154. https://doi.org/10.1016/j.cej.2019.05.078
48. Lavin-lopez MP, Paton-carrero A, Sanchez-silva L, et al. (2017) Influence of the reduction strategy in the synthesis of reduced graphene oxide. *Adv Powder Technol* 28: 3195–3203. https://doi.org/10.1016/j.apt.2017.09.032
49. Oberdick SD, Abdelgaw A, Moya C, et al. (2018) Spin canting across core/shell Fe_3O_4/$Mn_xFe_{3-x}O_4$ nanoparticles. *Sci Rep* 8: 1–12. https://doi.org/10.1038/s41598-018-21626-0
50. Korsakova AS, Kotsikau DA, Haiduk YS, et al. (2020) Synthesis and physicochemical properties of $Mn_xFe_{3-x}O_4$ solid solutions. *Condens Matter Interphases* 22: 466–472. https://doi.org/10.17308/kcmf.2020.22/3076
51. Amighian J, Karimzadeh E, Mozaffari M (2013) The effect of Mn^{2+} substitution on magnetic properties of $Mn_xFe_{3-x}O_4$ nanoparticles prepared by coprecipitation method. *J Magn Magn Mater* 332: 157–162. https://doi.org/10.1016/j.jmmm.2012.12.005
52. Yang X, Niu Y, Li Q, et al. (2018) The influence of fabrication methods on structure and microwave absorption property of Fe_3O_4/rGO composites. *J Supercond Nov Magn* 31: 2841–2849. https://doi.org/10.1007/s10948-017-4552-0
53. Wickham DG (1969) The chemical composition of spinels in the system $Fe_3O_4Mn_3O_4$. *J Inorg Nucl Chem* 31: 313–320. https://doi.org/10.1016/0022-1902(69)80474-4
54. Taufiq A, Sunaryono, Putra EGR, et al. (2015) Nano-structural studies on Fe_3O_4 particles dispersing in a magnetic fluid using X-ray diffractometry and small-angle neutron scattering. *Mater Sci Forum* 827: 213–218. https://doi.org/10.4028/www.scientific.net/MSF.827.213
55. Rowley-Neale SJ, Randviir EP, Abo Dena AS, et al. (2018) An overview of recent applications of reduced graphene oxide as a basis of electroanalytical sensing platforms. *Appl Mater Today* 10: 218-226. https://doi.org/10.1016/j.apmt.2017.11.010
56. Smith AT, LaChance AM, Zeng S, et al. (2019) Synthesis, properties, and applications of graphene oxide/reduced graphene oxide and their nanocomposites. *Nano Mater Sci* 1: 31–47. https://doi.org/10.1016/j.nanoms.2019.02.004
57. Wang Y, Gao X, Wu X, et al. (2018) Hierarchical $ZnFe_2O_4$@RGO@CuS composite: Strong absorption and wide-frequency absorption properties. *Ceram Int* 44: 9816–9822. https://doi.org/10.1016/j.ceramint.2018.02.220
58. Ding Y, Zhang L, Liao Q, et al. (2016) Electromagnetic wave absorption in reduced graphene oxide functionalized with Fe_3O_4/Fe nanorings. *Nano Res* 9: 2018–2025. https://doi.org/10.1007/s12274-016-1092-z
59. Daisuke K, Sugano S, Kosugi Y, et al. (2019) Selective growth of α-Fe_2O_3, γ-Fe_2O_3 and Fe_3O_4 at low-temperatures and under ambient pressure. *Jpn J Appl Phys* 58: 095504. https://doi.org/10.7567/1347-4065/ab39d1
60. Kakavandi B, Jonidi A, Rezaei R, et al. (2013) Synthesis and properties of Fe_3O_4-activated carbon magnetic nanoparticles for removal of aniline from aqueous solution: equilibrium, kinetic and thermodynamic studies. *Iranian J Environ Health Sci Eng* 10: 19. https://doi.org/10.1186/1735-2746-10-19
61. Juang RS, Yei YC, Liao CS, et al. (2018) Synthesis of magnetic Fe_3O_4/activated carbon nanocomposites with high surface area as recoverable adsorbents. *J Taiwan Inst Chem Eng* 90: 51–60. https://doi.org/10.1016/j.jtice.2017.12.005

62. Bagheri S, Muhd Julkapli N, Bee Abd Hamid S (2015) Functionalized activated carbon derived from biomass for photocatalysis applications perspective. *Int J Photoenergy* 2015: 1–30. https://doi.org/10.1155/2015/218743
63. Olad A, Gharekhani H (2016) Study on the capacitive performance of polyaniline/activated carbon nanocomposite for supercapacitor application. *J Polym Res* 23: 147. https://doi.org/10.1007/s10965-016-1031-4
64. Yin P, Deng Y, Zhang L, et al. (2018) Facile synthesis and microwave absorption investigation of activated carbon@Fe_3O_4 composites in the lowfrequency band. *RSC Adv* 8: 23048–23057. https://doi.org/10.1039/C8RA04141E
65. Yin P, Deng Y, Zhang L, et al. (2018) The microwave absorbing properties of ZnO/Fe_3O_4/paraffin composites in low-frequency band. *Mater Res Express* 2: 026109. https://doi.org/10.1088/2053-1591/aaae58
66. Wang Z, Wu L, Zhou J, et al. (2014) Chemoselectivity-induced multiple interfaces in MWCNT/Fe_3O_4@ZnO heterotrimers for whole X-band microwave absorption. *Nanoscale* 6: 12298–12302. https://doi.org/10.1039/C4NR03040K
67. Shu R, Zhang G, Zhang J, et al. (2018) Fabrication of reduced graphene oxide/multi-walled carbon nanotubes/zinc ferrite hybrid composites as high-performance microwave absorbers. *J Alloys Compd* 736: 1–11. https://doi.org/10.1016/j.jallcom.2017.11.084
68. Jian X, Wu B, Wei Y, et al. (2016) Facile synthesis of Fe_3O_4/GCs composites and their enhanced microwave absorption properties. *ACS Appl Mater Interfaces* 8: 6101–6109. https://doi.org/10.1021/acsami.6b00388
69. Salem DMSA, Ismail MM, Aly-Eldeen MA (2019) Biogenic synthesis and antimicrobial potency of iron oxide (Fe_3O_4) nanoparticles using algae harvested from the Mediterranean Sea, Egypt. *Egypt J Aquat Res* 45: 197–204. https://doi.org/10.1016/j.ejar.2019.07.002
70. Tajik S, Askari MB, Ahmadi SA, et al. (2022) Electrochemical sensor based on $ZnFe_2O_4$/RGO nanocomposite for ultrasensitive detection of hydrazine in real samples. *Nanomaterials* 12: 491. https://doi.org/10.3390/nano12030491
71. Cao WQ, Wang XX, Yuan J, et al. (2015) Temperature dependent microwave absorption of ultrathin graphene composites. *J Mater Chem C* 3: 10017–10022. http://dx.doi.org/10.1039/C5TC02185E
72. Qiao Y, Xiao J, Jia Q, et al. (2019) Preparation and microwave absorption properties of $ZnFe_2O_4$/polyaniline/graphene oxide composite. *Results Phys* 13: 102221. https://doi.org/10.1016/j.rinp.2019.102221
73. Cao M, Wang X, Cao W, et al. (2018) Thermally driven transport and relaxation switching self-powered electromagnetic energy conversion. *Small* 14: 1800987. https://doi.org/10.1002/smll.201800987
74. Shu R, Zhang J, Guo C, et al. (2020) Facile synthesis of nitrogen-doped reduced graphene oxide/nickel-zinc ferrite composites as high-performance microwave absorbers in the X-band. *Chem Eng J* 384: 123266. https://doi.org/10.1016/j.cej.2019.123266
75. Chen C, Xi J, Zhou E, et al. (2017) Porous graphene microflowers for high-performance microwave absorption. *Nano-Micro Lett* 10: 26. https://doi.org/10.1007/s40820-017-0179-8
76. Wen B, Cao MS, Hou ZL, et al. (2013) Temperature dependent microwave attenuation behavior for carbon-nanotube/silica composites. *Carbon N Y* 65: 124–139. https://doi.org/10.1016/j.carbon.2013.07.110

77. Liang LL, Song G, Liu Z, et al. (2020) Constructing $Ni_{12}P_5/Ni_2P$ heterostructures to boost interfacial polarization for enhanced microwave absorption performance. *ACS Appl Mater Interfaces* 12: 52208–52220. https://doi.org/10.1021/acsami.0c16287
78. Ding J, Wang L, Zhao Y, et al. (2019) Boosted interfacial polarization from multishell TiO_2@Fe_3O_4@PPy heterojunction for eenhanced microwave absorption. *Small* 15: 1902885. https://doi.org/10.1002/smll.201902885
79. Jabir MS, Nayef UM, Abdulkadhim WK, et al. (2019) Supermagnetic Fe_3O_4-PEG nanoparticles combined with NIR laser and alternating magnetic field as potent anti-cancer agent against human ovarian cancer cells. *Mater Res Express* 6: 115412. https://doi.org/10.1088/2053-1591/ab50a0
80. Idris F, Hashim M, Abbas Z, et al. (2016) Recent developments of smart electromagnetic absorbers based polymer-composites at gigahertz frequencies. *J Magn Magn Mater* 405: 197–208. https://doi.org/10.1016/j.jmmm.2015.12.070
81. Sun D, Zou Q, Wang Y, et al. (2014) Controllable synthesis of porous Fe_3O_4@ZnO sphere decorated graphene for extraordinary electromagnetic wave absorption. *Nanoscale* 6: 6557–6562. https://doi.org/10.1039/C3NR06797A
82. Yotsomnuk P, Skolpap W (2017) Biofuel production from waste virgin coconut oil by hydrocracking over HZSM-5 zeolite. *IJASET* 5: 54–57. Available from: http://ijaseat.iraj.in/paper_detail.php?paper_id=7992
83. Al-Muttaqii M, Kurniawansyah F, Prajitno DH, et al. (2019) Bio-kerosene and bio-gasoil from coconut oils via hydrocracking process over Ni-Fe/HZSM-5 catalyst. *Bull Chem React Eng Catal* 14: 309–319. https://doi.org/10.9767/bcrec.14.2.2669.309-319
84. Nouri Parouch A, Koukabi N, Abdous E (2020) Tetrazole derivatives synthesis using Fe_3O_4@fibroin-SO_3H as a magnetically separable green solid acid nanocatalyst under solvent-free conditions. *Res Chem Intermed* 46: 3295–3310. https://doi.org/10.1007/s11164-020-04131-w
85. Mostafatabar AH, Bahlakeh G, Ramezanzadeh B (2022) Novel bi-functional RGO-HPSE-Zn@epoxy nanocomposite with superior corrosion protection potency. *J Ind Eng Chem* 108: 28–46. https://doi.org/10.1016/j.jiec.2021.12.022

AIMS Press